

Part III

Risley-Prism-Based Beam-Steering Systems

Chapter 7

Exact and Approximate Solutions for Risley-Prism-Based Beam-Steering Systems in Different Configurations

Risley prisms are pairs of rotatable prisms that can be used to continuously scan a laser beam over a wide angular range with a high resolution. Risley prisms are particularly useful in optical tracking and pointing a target in free space

Chapters 7 through 10 are the four Chapters in Part III of this book and devoted to a discussion of Risley-prism-based beam-steering systems (i.e., rotating wedge prism scanning systems), which have two basic problems in practical application. Chapter 7 considers the exact and approximate solutions of first problem, i.e., given the two prisms' orientations, in what direction does the laser beam propagate after emerging from the system? Chapters 8 and 9 consider the second problem, which may be regarded as the inverse of the first one, i.e., given the required pointing position, what will be the orientations of the prisms? Prism systems in these three Chapters are considered error-free: no prism tilt and no beam and mechanical axes misalignment, which will be considered in Chapter 10 of this book.

Optical Prisms are ideal for ray deviation. Refractive prism (the “prism” for short) is one type of the optical prisms for redirecting light at a designated angle. [7.1] Refractive prisms for steering optical beams are usually the wedge-type prisms, whose principal section is a right triangle and can be divided into three types according to degrees of their opening angle (see, e.g., Fig. 7.1).

- The wedge prism is a prism with a shallow wedge angle that is a few degrees, for which the first-order approximation may predict results with sufficient accuracy in some applications. [7.2] Wedge prisms are used in Risley prism pointer for high speed pointing and tracking of remote target.

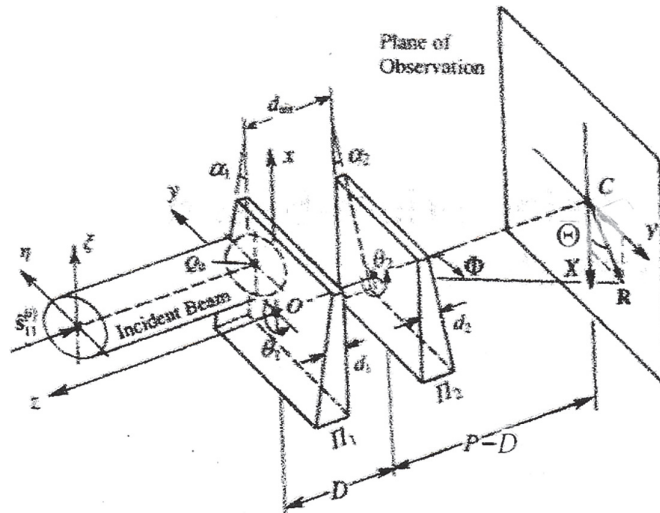


Figure 7.1 Schematic diagram illustrating the notation and coordinate systems for tracing of the ray path transverse the prisms. The incident beam is collinear with the z axis, which is also the axis of rotation of the two prisms Π_1 and Π_2 of indices n_1 and n_2 and the prism angles α_1 and α_2 , respectively.

- The thin prism is a prism whose prism angle is larger than that for a wedge prism but less than 10° , for which the third-order approximation may predict results with sufficient accuracy in some applications. [7.3] Thin prisms are used in Risley prism pointer for eye examination and laser beam pointing and tracking of remote target.
- Thick prism (or wide-angle achromatic prism, or large-deviation achromatic prism) is a prism whose prism angle can be up to 30° or even greater. Thick prisms are used in Risley prism scanners when large field-of-regard (FOR) is required, such as the infrared countermeasure (IRCM) systems for protecting aircrafts from infrared guided missile threat [7.4–7.7] and airborne infrared guided search-and-rescue operations [7.8].

The equations to be derived in part III of this book are mainly for thick prisms, which represent exact solution to the refracting power of the prisms of any opening angle. Risley scanners using wedge or thin prisms will be considered as special cases of the slightly tedious equations for the thick prism scanners.

7.1 Historical Introduction

For a physical diagnosis of the binocular accommodation, i.e., to measure the ability of moving the optical axes of the two eyes to converge on nearby objects, eye doctors use a moving light spot produced by an optical device

consisting of two thin prisms of equal power that can be rotated in opposite orientations in their own plane. Such a device, known as the Risley prism, is the equivalent of a single prism of variable power. (see, e.g., [7.4] and references cited therein). Beyond the area of eye examination, Risley prism pair has found applications to quite a few areas. [7.10]

Since the 1980s, there were increasing demands for compact, robust and less expensive devices of beam steering for aiming laser beams at distant targets. [7.11, 7.12] Typical commercial methods of beam-steering are the single mirror and the two-mirror/two-axis systems that use, respectively, gimbaled mirror or the orthogonal Galvanometric modules [see, e.g., chapters 5 and 6]. More recently, attention has been paid to Risley prisms because of the following favorable features they may have:

- Robustness: relatively insensitive to vibrations;
- Compactness: simple opto-mechanics: a nearly straight optical path traversing two prisms supported by their respective ball-bearing guides with low friction and wobble, all packaged in a long and thin configuration;
- Acceptance of the laser beam up to 6 mm in diameter and 4 in of optical beams for $\pm 60^\circ$ angular range with 1mrad pointing accuracy;
- Usually, less power consumptions than mirror scanning devices.

With a significant improvement in the angular operational range and pointing accuracy, the applications for the Risley prism have been steadily expanding from eye examinations to laser-beam pointing and to image-guided surgery using endoscopic laser scalpel. [7.13,7.14] and to interferometry and microscopy [7.15, 7.16].

In addition to the obvious disadvantages, such as its inherent chromatic aberration, Fresnel reflection losses and wavefront distortions, Risley prisms have the following imperfect features:

- The ratios between the ray deviation and between the optical and mechanical scan angles is governed by Snell's law, that brings a non-linear relationship to beam steering and prism rotation angles and leads a few adverse issues (e.g., scan blind zone and control singularity) to beam steering performance in double-prism Risley systems.
- Straight line scan patterns, including raster scan pattern, generated by Risley prism pairs are usually very poor in scan linearity.
- Coverage of all pointing angles can only be achieved when the pair of prisms is exactly matched. If there is any difference, even very small, in prism opening angle, index of refraction, or system alignment, there will be a small area where the prisms cannot point at.

- Risley prism pointers are practically limited in field-of-regard (FOR) because the mass of the two rotating prisms increases drastically with the prism angle and aperture diameter.

Risley prism pair, with rotatable prisms, can be used to continuously steer a laser beam over a wide angular range with high resolution [7.9, 7.10], and is particularly useful for tracking and pointing a target and also for producing many interesting sets of scan patterns on observation plane. Figure 7.1 is a schematic diagram showing the beam steering geometry, in which the two prisms Π_1 and Π_2 may have different indices n_1 and n_2 and different angles of prism (i.e., the prism opening angle or the apex angle) α_1 and α_2 . By controlling the orientations, rate of rotation, and phasing of Π_1 and Π_2 , different scan patterns can be generated [7.17–7.20]. The thin prism approximation has been used for a first-order analysis, and it is found that the key parameter for the scan pattern generated by a pair of rotating prisms in the air is given by [7.18, 7.19]

$$\delta_q = (n_q - 1)\alpha_q \quad (q = 1, 2), \quad (7.1)$$

which represents the first-order approximation to the general expression of the minimum deviation angle between the emergent and incident rays of a single prism; this angle defines the parameter for an estimation of the power of the prism in the ray refraction. [7.19].

It is worth of noting that the two prisms shown in Fig. 7.1 are able of rotating in their own plane around the z axis, one may change this motion mode from prisms rotating to titling, e.g., the first prism Π_1 can be tilted around the y axis and the second prism Π_2 , after a rotation around the z axis for 90° , can be tilted around the x axis. After a careful design of their driving functions, both the rotating and the titling double prisms can be used for laser beam steering for precise pointing [7.20, 7.21]. A comparison of the angular range, the speed and pointing accuracy of mechanical laser beam steering systems, including the single mirror, two-axis/two-mirror and Risley prisms, can be found in [7.22]. Further, a comparison of the scan angles of mechanical beam steering with the non-mechanical steering using liquid crystal plates can be found in [7.23].

This chapter is organized as follows. Analytic ray-tracing of a ray through a two-prism system is performed in the Section 7.2 to develop an exact theory of thick prisms working in the error-free conditions, i.e., no prism tilt and no beam and mechanical axes misalignment. The exact solution of the scan field is obtained and then applied to a structural analysis of the fields of rays inside and outside the double prisms system. After that, the exact solution is expanded into a power series of δ_q to give the closed-form approximations. Accuracy of the predictions of the approximation theories of different order are compared numerically, and the optical distortion in the scan pattern is

investigated within the accuracy of third-order theory. Section 7.3 considers the power of ray deviation by the Risley prisms of different configurations and the influence of the effect of the total internal reflection (TIR) on the range of the total angle of deviation and the development of the TIR induced system operation breakdown. [7.24]

The main reference of this chapter is Ref. [7.9].

7.2 Exact and Approximate Expressions for Risley-Prism-Based Beam Steering Systems

Figure 7.1 shows three coordinate systems for ray tracing, i.e.,

- System (x, y, z) with the triad $(\hat{\mathbf{i}}, \hat{\mathbf{j}}, \hat{\mathbf{k}})$ provides a frame for the ray tracing.
- System (ξ, η) on the plane of incidence defines the incoming beam profile.
- System (X, Y) for the plane of observation displays the scan pattern.

7.2.1. Combinations of prisms for beam steering

The two prisms Π_1 and Π_2 are arranged with an air gap d_{air} between their flat sides, which are perpendicular to the z axis that is also the axis of the two rotary prisms. The first surface of Π_1 (i.e., surface 11) intersects the z axis at the point O that is the origin of the (x, y, z) system. The thicknesses of Π_1 and Π_2 are, respectively, d_1 and d_2 as measured along the z axis. Rotations of the two prisms are described by

$$\theta_q = \omega_q t + \theta_{0q} \quad (q = 1, 2), \quad (7.2)$$

where t denotes the time, ω_1 and ω_2 are the angular frequencies of rotation, and θ_{01} and θ_{02} are the initial phase angles. Assume $\theta_{01} = \theta_{02} = 0$ in all numerical calculations unless otherwise stated. To show the analytic expressions more explicitly, the following symbols will be used:

$$D = d_1 + d_{\text{air}} + d_2, \quad D_n = \frac{d_1}{n_1} + d_{\text{air}} + \frac{d_2}{n_2}, \quad (7.3)$$

and the ratio of the prisms' rotation angular frequencies

$$m = \omega_2 / \omega_1. \quad (7.4)$$

The suffixes 11, 12, 21, and 22 are attached to the ray and direction vectors to indicate their pertinence to the first or the second surface of the prisms Π_1 or Π_2 .

Consider a single beam propagating in the direction specified by the unit (ray) vector $\hat{\mathbf{s}}_{11}^{(i)} = (0, 0, -1)$ to the first surface of the prism Π_1 . Within the accuracy of geometrical optics, we may describe the single beam by a bundle of collimated rays all in the direction perpendicular to the xy plane, and the beam axis passes through the point $Q_0(x_0, y_0)$ (see Fig. 7.1). In the case of scanning an elliptical beam with the major and minor axes ξ_0 and η_0 , we may express the beam of incidence parametrically in the form

$$\xi = x_0 + \xi_0 \cos \tau \quad \text{and} \quad \eta = y_0 + \eta_0 \sin \tau, \quad (7.5)$$

where τ is a parameter running from 0 to 2π , and $\xi = \eta = 0$ in case of a ray propagating along the z axis.

A number of publications [7.18,7.19] have shown the linear theory about the scan pattern scanned out by a single ray through a pair of rotatable thin lens on the plane of observation located at a distance P away from the origin O of the coordinates (x, y, z) can be expressed in the (X, Y) coordinates system as

$$\begin{pmatrix} X \\ Y \end{pmatrix} = P \left[\delta_1 \begin{pmatrix} \cos \theta_1 \\ \sin \theta_1 \end{pmatrix} + \delta_2 \begin{pmatrix} \cos \theta_2 \\ \sin \theta_2 \end{pmatrix} \right], \quad (7.6)$$

where $\delta_1 = (n_1 - 1) \alpha_1$ and $\delta_2 = (n_2 - 1) \alpha_2$ according to Eq. (7.1) for the angular deviation of the thin prisms. Besides, Eq. (7.2) assumes that the plane of observation is perpendicular to the axis of the system and located in the far-field region (i.e., the region where $P \gg D$). Further, we may use the complex vector to express Eq. (7.6) more concisely in the form

$$\mathbf{R}_{1F} = X + \mathbf{i}Y = P[\delta_1 \exp(\mathbf{i}\theta_1) + \delta_2 \exp(\mathbf{i}\theta_2)], \quad (7.7)$$

where $\mathbf{i} = \sqrt{-1}$, and the subscript 1F stresses the fact that Eq. (7.7) is the first-order approximation of the scan pattern observed in the far-field region. Equation (7.7) will be referred to as the J&W formula, because the classic textbook [7.19] by Jenkins and White provides easy access to this first-order far-field-region formula for the scan pattern may be produced by Risley prism.

7.2.2 Analytic ray-tracing of a ray though a pair of thick prisms

For simplicity, we start at a beam incidence from the point z_0 located on the z -axis specified by the position vector

$$\mathbf{r}_{10} = (\xi, \eta, z_{10}). \quad (7.8)$$

The rectilinear propagation of the ray in the direction specified by $\hat{\mathbf{s}}_{11}^{(i)} = (0, 0, -1)$ allows us to express the incidence to the system in the form

$$\hat{\mathbf{s}}_{11}^{(i)} \times (\mathbf{r} - \mathbf{r}_{10}) = 0, \quad (7.9)$$

where $\mathbf{r} = (x, y, z)$ is the position vector for a variable point.

The ray of incidence strikes the surface 11 of prism Π_1 that is now in the position specified by its surface normal

$$\hat{\mathbf{n}}_{11} = (\sin \alpha_1 \cos \theta_1, \sin \alpha_1 \sin \theta_1, \cos \alpha_1) \quad (7.10a)$$

from which the surface normal of the surface 22 of prism Π_2 , given by

$$\hat{\mathbf{n}}_{22} = \hat{\mathbf{n}}_{11}|_{\theta_1 \rightarrow \pi + \theta_1} = (-\sin \alpha_1 \cos \theta_1, -\sin \alpha_1 \sin \theta_1, \cos \alpha_1). \quad (7.10b)$$

Furthermore, the origin O of the coordinates (x, y, z) system is at the center of surface 11, we may express surface 11 as [see, e.g., Eq. (A7) in the Appendix A]

$$\hat{\mathbf{n}}_{11} \cdot \mathbf{r} = 0. \quad (7.11)$$

In general, Eqs. (7.9) and (7.11) can be solved simultaneously for the position vector \mathbf{r}_{11} to ascertain where the incident beam strikes surface 11, at which the beam is refracted into the direction specified by the direction vector $\hat{\mathbf{s}}_{11}^{(i)(r)} = (k_{11}^{(r)}, l_{11}^{(r)}, m_{11}^{(r)})$. The two direction vectors $\hat{\mathbf{s}}_{11}^{(i)}$ and $\hat{\mathbf{s}}_{11}^{(r)}$ for the incident and refracted ray at the surface 11 are coupled by the Snell's law [see, Eq. (1.15)]. Replacing $(\hat{\mathbf{s}}_{11}^{(i)}, \hat{\mathbf{s}}^{(r)}, \hat{\mathbf{n}}, n_1, n_2)$ in Eq. (1.5) by $(\hat{\mathbf{s}}_{11}^{(i)}, \hat{\mathbf{s}}_{11}^{(r)}, \hat{\mathbf{n}}_{11}, 1, n_1)$, we are able to describe the direction of the ray refracted from the air into the first prism Π_1 as

$$\hat{\mathbf{s}}_{11}^{(r)} = \frac{1}{n_1} [\hat{\mathbf{s}}_{11}^{(i)} - (\hat{\mathbf{n}}_{11} \cdot \hat{\mathbf{s}}_{11}^{(i)}) \hat{\mathbf{n}}_{11}] - (\hat{\mathbf{n}}_{11}) \sqrt{1 - \left(\frac{1}{n_1}\right)^2 + \left(\frac{1}{n_1}\right)^2 (\hat{\mathbf{n}}_{11} \cdot \hat{\mathbf{s}}_{11}^{(i)})^2}, \quad (7.12)$$

or, more explicitly as

$$\hat{\mathbf{s}}_{11}^{(r)} = \frac{1}{n_1} (\hat{\mathbf{s}}_{11}^{(i)} - A_1 \hat{\mathbf{n}}_{11}),$$

where $A_1 = F_1 + \sqrt{n_1^2 - 1 + F_1^2}$ and $F_1 = \hat{\mathbf{s}}_{11}^{(i)} \cdot \hat{\mathbf{n}}_{11}$.

Equations (7.8)–(7.11) describe the ray propagation from the object point \mathbf{r}_{10} to the surface 11; the formats of these equations can describe the ray propagation from surface 11 to surface 12 if the subscripts 10 and 11 are replaced by 11 and 12. After that, we are ready to deal with the ray refraction at the boundary surface 12 where the ray direction vectors $\hat{\mathbf{s}}_{12}^{12}$ and $\hat{\mathbf{s}}_{12}^{(r)}$

describing the refraction at the boundary from the glass to the air are now coupled by the Snell's law in Eq. (1.15) under the condition of $n_2 = 1$, i.e.,

$$\hat{\mathbf{s}}_{12}^{(r)} = n_1 [\hat{\mathbf{s}}_{11}^{(r)} - (\hat{\mathbf{n}}_{12} \cdot \hat{\mathbf{s}}_{11}^{(r)}) \hat{\mathbf{n}}_{12}] - (\hat{\mathbf{n}}_{12}) \sqrt{1 - n_1^2 + n_1^2 (\hat{\mathbf{n}}_{12} \cdot \hat{\mathbf{s}}_{11}^{(r)})^2}. \quad (7.13)$$

or, more explicitly as

$$\hat{\mathbf{s}}_{12}^{(r)} = n_1 (\hat{\mathbf{s}}_{12}^{(i)} - A_2 \hat{\mathbf{n}}_{12}),$$

where $A_2 = n_1 F_2 + \sqrt{1 - n_1^2 + n_1^2 F_2^2}$ with $F_2 = \hat{\mathbf{n}}_{12} \cdot \hat{\mathbf{s}}_{11}^{(r)}$ and $\hat{\mathbf{n}}_{12} = (0, 0, 1)$. The directions of the rays in the Risley prism are summarized in Table 7.1.

Applying the same formulation and sign convention, we may trace the ray path over the air gap to the first surface 21 of the second prism Π_2 , where we obtain expressions for the direction vectors of the ray propagating from the surface 21 to the surface 22, for which we also found the locations of the points specified by the position vector $\mathbf{r}_{22} = (x_{22}, y_{22}, z_{22})$, from where the ray refracted off the scanner in the direction specified by direction vector $\hat{\mathbf{s}}_{22}^{(i)} = (k_{22}^{(i)}, l_{22}^{(i)}, m_{22}^{(i)})$ that is found expressible in the form

Table 7.1 Expressions of the direction vectors of ray refractions in the Risley prism in the TV-VT (i.e., the A-1) configuration as shown in Figs. 7.1 and 7.7(a). Assume the ray of incidence along the z-axis to the center of prism Π_1 , i.e., $\hat{\mathbf{s}}_{11}^{(i)} = (0, 0, -1)$.

Prism	Surface	Ray Unit Vector	Direction Cosines	Expressions: $a_1 = (\cos \alpha_1 - \sqrt{n_1^2 - \sin^2 \alpha_1}) \sin \alpha_1$
Π_1	11	$\hat{\mathbf{s}}_{11}^{(r)}$	$k_{11}^{(r)} =$	$(a_1/n_1) \cos \theta_1$
			$l_{11}^{(r)} =$	$(a_1/n_1) \sin \theta_1$
			$m_{11}^{(r)} =$	$-\sqrt{1 - (k_{11}^{(r)})^2 - (l_{11}^{(r)})^2} = -\sqrt{1 - (a_1/n_1)^2}$
	12	$\hat{\mathbf{s}}_{12}^{(r)}$	$k_{12}^{(r)} =$	$a_1 \cos \theta_1$
			$l_{12}^{(r)} =$	$a_1 \sin \theta_1$
			$m_{12}^{(r)} =$	$-\sqrt{1 - (k_{12}^{(r)})^2 - (l_{12}^{(r)})^2} = -\sqrt{1 - a_1^2}$
Π_2	21	$\hat{\mathbf{s}}_{21}^{(r)}$	$k_{21}^{(r)} =$	$(a_1/n_2) \cos \theta_1$
			$l_{21}^{(r)} =$	$(a_1/n_2) \sin \theta_1$
			$m_{21}^{(r)} =$	$-\sqrt{1 - (k_{21}^{(r)})^2 - (l_{21}^{(r)})^2} = -\sqrt{1 - (a_1/n_2)^2}$
	22	$\hat{\mathbf{s}}_{22}^{(r)}$	$k_{22}^{(r)} =$	See Eq. (7.14)
			$l_{22}^{(r)} =$	
			$m_{22}^{(r)} =$	

$$\left. \begin{aligned} k_{22}^{(r)} &= \sin \alpha_1 (\cos \alpha_1 - \sqrt{n_1^2 - \sin^2 \alpha_1}) \cos \theta_1 + A_1 \sin \alpha_2 \cos \theta_2, \\ l_{22}^{(r)} &= \sin \alpha_1 (\cos \alpha_1 - \sqrt{n_1^2 - \sin^2 \alpha_1}) \sin \theta_1 + A_1 \sin \alpha_2 \sin \theta_2, \\ m_{22}^{(r)} &= -\sqrt{n_2^2 - n_1^2 + [\sin^2 \alpha_1 + \cos \alpha_1 \sqrt{n_1^2 - \sin^2 \alpha_1}]^2} - A_1 \cos \alpha_2 \end{aligned} \right\}, \quad (7.14)$$

where

$$\begin{aligned} A_1 &= \sqrt{1 - n_2^2 + \left[\cos \alpha_2 \sqrt{n_2^2 - n_1^2 + [\sin^2 \alpha_1 + \cos \alpha_1 \sqrt{n_1^2 - \sin^2 \alpha_1}]^2} \right.} \\ &\quad \left. + \sin \alpha_1 \sin \alpha_2 (\cos \alpha_1 - \sqrt{n_1^2 - \sin^2 \alpha_1}) \cos(\theta_2 - \theta_1) \right]^2} \\ &\quad - \cos \alpha_2 \sqrt{n_2^2 - n_1^2 + [\sin^2 \alpha_1 + \cos \alpha_1 \sqrt{n_1^2 - \sin^2 \alpha_1}]^2} \\ &\quad - \sin \alpha_1 \sin \alpha_2 (\cos \alpha_1 - \sqrt{n_1^2 - \sin^2 \alpha_1}) \cos(\theta_2 - \theta_1). \end{aligned}$$

The scan vector \mathbf{R} is a variable vector with one end at the point specified by the position vector \mathbf{r}_{22} and another end depicting a scan pattern on the observation plane located at $z = P$, as illustrated in Fig. 1.4 and expressed in Eq. (1.12), which can now be re-expressed in the form

$$\mathbf{R} = \mathbf{r}_{22} - \frac{P + \hat{\mathbf{e}}_Z \cdot \mathbf{r}_{22}}{\hat{\mathbf{e}}_Z \cdot \hat{\mathbf{s}}_{22}^{(r)}} \hat{\mathbf{s}}_{22}^{(r)}, \quad (7.15)$$

where $\hat{\mathbf{e}}_Z$ is the normal vector to the plane of observation (see Fig. 7.1), and \mathbf{r}_{22} is a function of the parameters regarding the scanning geometry and incident beam profile as shown in Eqs. (7.20) and (7.21). However, $|\mathbf{r}_{22}|$ becomes a negligible quantity in the far-field region where $P \gg D$. Under this condition, all of the terms containing \mathbf{r}_{22} on right side of Eq. (7.15) can be discarded. To reflect on the structural difference in the near and far-regions scan field, we may split \mathbf{R} in Eq. (7.15) into two parts as

$$\mathbf{R} = \mathbf{R}_F + \Delta \mathbf{R}_N, \quad (7.16)$$

where

$$\mathbf{R}_F = -P \left(\frac{\hat{\mathbf{s}}_{22}^{(r)}}{\hat{\mathbf{e}}_Z \cdot \hat{\mathbf{s}}_{22}^{(r)}} \right) \text{ and } \Delta \mathbf{R}_N = \left(\mathbf{r}_{22} - \frac{\hat{\mathbf{e}}_Z \cdot \mathbf{r}_{22}}{\hat{\mathbf{e}}_Z \cdot \hat{\mathbf{s}}_{22}^{(r)}} \hat{\mathbf{s}}_{22}^{(r)} \right). \quad (7.17)$$

\mathbf{R}_F represents the scan pattern as observed in the far-field region, and $\Delta \mathbf{R}_N$ represents the contributions of the scanning geometry parameters (D , D_n) and

the incident beam parameters (ξ, η) to the filed structure, which are the non-negligible accounts in the near-field region, where Eq. (7.15) gives correct results of the scan pattern.

After substituting from Eq. (7.14) into Eq. (7.17), we are able to express the scan pattern on the plane of observation in the far-field region parametrical in the form

$$\begin{pmatrix} X_F \\ Y_F \end{pmatrix} = P \begin{pmatrix} F_X(\theta_1, \theta_2) \\ F_Y(\theta_1, \theta_2) \end{pmatrix}, \quad (7.18)$$

where

$$\begin{bmatrix} F_X(\theta_1, \theta_2) \\ F_Y(\theta_1, \theta_2) \end{bmatrix} = \frac{\sin \alpha_1 (\cos \alpha_1 - \sqrt{n_1^2 - \sin^2 \alpha_1}) \begin{pmatrix} \cos \theta_1 \\ \sin \theta_1 \end{pmatrix} + A \sin \alpha_2 \begin{pmatrix} \cos \theta_2 \\ \sin \theta_2 \end{pmatrix}}{-\sqrt{n_2^2 - n_1^2 + \left[\sin^2 \alpha_1 + \cos \alpha_1 \sqrt{n_1^2 - \sin^2 \alpha_1} \right]^2} + A \cos \alpha_2}.$$

7.2.3 Scan field distribution over the interior of the Risley prism scanning system

Develop expressions for the scan fields produced by Risley prism pairs is a long and tedious process. To reduce the load of mathematical manipulations, let us consider the field distributions inside the Risley prism pairs in different configurations that may help us to find out their similarities and avoid unnecessary repetition. In addition, knowledge of scan field distributions inside the Risley prism pair will help us to understand how a Risley prism pointer suffers from blind zone and control singularities as will be detailed in subsequent discussion.

Figure 7.2(a) shows the results obtained from the graphical raytracing analysis shown in Fig. 7.2(b), in which the ray path through the Risley prism scanner in the A-1 configuration is shown under the assumption that along the z -axis of the scanner is a single ray (which may act on behalf of the axis of the beam of incidence) propagating to the scanner to produce a scan field inside this scanner when prisms rotate. Figures 7.2(a) and 7.2(b) show the scan field is a combination of three sections of axial symmetric circular cones of different parameters as indicated the cones #1, #2 and #3 in Fig. 7.2(a), in which $(\Theta_1, \Theta_2, \Theta_3)$ are their half-vertex angles and $(\Delta z_1, \Delta z_2, \Delta z_3)$ are the locations of their conic points on the z -axis in reference to the origin of Cartesian coordinates shown in Fig. 7.1.

Using the notation $\hat{\mathbf{s}}_{11}^{(r)} = (k_{11}^{(r)}, l_{11}^{(r)}, m_{11}^{(r)})$ and the expressions listed in the Table 7.1 for the ray refracted at the surface 11 of the first prism Π_1 , we may express the parameters of the right circular cone #1 in the form

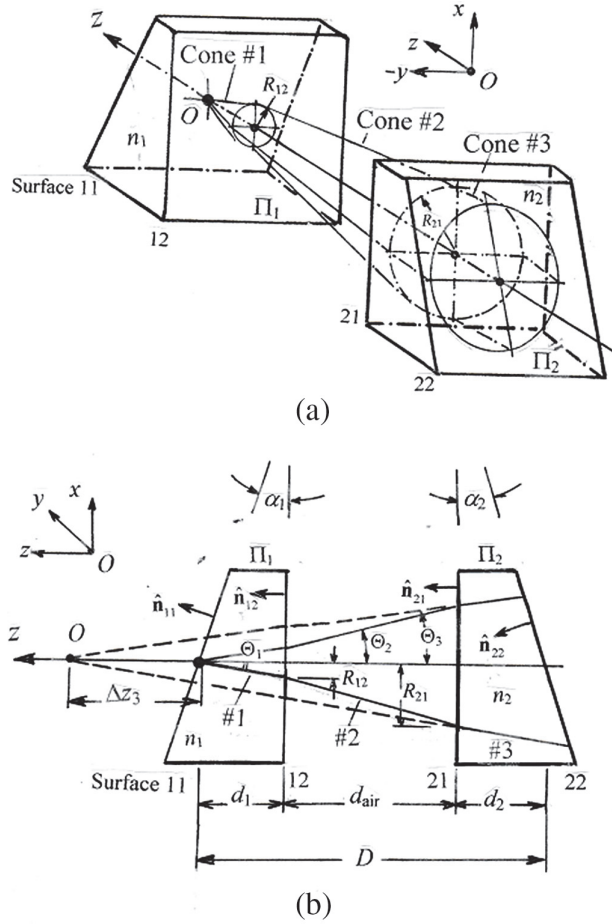


Figure 7.2 The fields of rays inside the Risley-prism scanner in TV-VT configuration. (a) Graphical projection of the three scan fields inside the Risley prism scanner (b) With the notation illustrated.

$$\left. \begin{aligned} \text{Half-vertex angle : } \Theta_1 &= \arctan \frac{\sqrt{(k_{11}^{(r)})^2 + (l_{11}^{(r)})^2}}{-m_{11}^{(r)}} = \arctan \left[\frac{a_1}{\sqrt{n_1^2 - a_1^2}} \right], \\ \text{Location of the vertex of the cone 1 on the } z \text{ axis: } \Delta z_1 &= 0 \end{aligned} \right\} \quad (7.19a)$$

The radius of the base circle of the cone 1 is $R_{12} = d_1 \tan \Theta_1$, that can be shown on a stationary plane immediately behind the surface 12 of the prism Π_1 . R_{12} remains a constant when the prism Π_1 rotates.

Similarly, we find the parameters for cone #2 in the air gap between the two flat surfaces of the first and the second prism Π_1 and Π_2 , given by

$$\left. \begin{aligned} \text{Half-vertex angle: } \Theta_2 &= \arctan \left[\frac{a_1}{\sqrt{1-a_1^2}} \right], \\ \text{Location of the vertex of the cone 2 on the } z\text{-axis } \Delta z_2 &= d_1 \left(\sqrt{\frac{n_1^2 - a_1^2}{1-a_1^2}} - 1 \right) \end{aligned} \right\}. \quad (7.19b)$$

The radius of the base circle on the surface 21 of the cone 2 is $R_{21} = R_{12} + d_{\text{air}} \tan \Theta_2$.

Again, the half-vertex angle of cone #3 in the second prism Π_2 is found in the form

$$\Theta_3 = \arctan \left[\frac{a_1}{\sqrt{n_2^2 - a_1^2}} \right], \quad (7.19c)$$

and the location of the cone #3 vertex on the z -axis, given by.

$$\Delta z_3 = d_1 \left(\sqrt{\frac{n_1^2 - a_1^2}{n_2^2 - a_1^2}} - 1 \right) + d_{\text{air}} \left(\sqrt{\frac{n_1^2 - a_1^2}{1-a_1^2}} - 1 \right), \quad (7.19d)$$

and in case of using matched pairs, $n_1 = n_2$, Eq. (7.19d) reduces to

$$\Delta z_3 = d_{\text{air}} \left(\sqrt{\frac{n_1^2 - a_1^2}{1-a_1^2}} - 1 \right), \quad (7.19e)$$

The parameters shown in Eqs. (7.19a)–(7.19d) are independent from orientation of prisms. The intersection curve of cone #3 and surface 22 of the second prism is an ellipse for which the half-minor-axis is $R_{21} + d_2 \tan \Theta_3$ and half-major-axis, given by $R_{21} + d_2 \tan \Theta_3 / \cos \alpha_2$.

Equations. (7.19a)–(7.19d) become much simpler when the refractive indexes of two prisms $n_1 = n_2$. In this case, the two plane surfaces on the two sides of the air gap in the configuration shown in Fig (7.1) do not affect the direction of the ray propagating over this gap, and we have the two ray direction vector $\hat{\mathbf{s}}_{11}^{(r)} = \hat{\mathbf{s}}_{21}^{(r)}$ and the two half-vertex angles $\Theta_1 = \Theta_3$. This is because when a ray traverses an air gap between two plane surfaces that are parallel to each other, it emerges parallel to its original direction but with a lateral displacement (see, e.g., Section 14.10 in [7.19]).

Based on the analysis presented above, we are able to show in Fig. 7.3 an example about two prism scanning systems with different configurations that may generate identical scan fields and scan patterns. Specifically, the two systems are $(\Pi_1 + \Pi_2)$ and $(\Pi_1' + \Pi_2)$, in which prism Π_1 in the first system is shown by the solid line in Fig. 7.3, which is replaced by the prism Π_1' in the second system, that is shown by the dash line in Fig. 7.3, whereas the second prism Π_2 in Fig. 7.3 remains the same in two systems.

Specification parameters (α_1, n_1) of the first prism Π_1 in the first system are different from (α_1', n_1') for the first prism Π_1' in the second system. Correct selection of (α_1', n_1') allows prism Π_1' in the second system to generate right circular cone 3 identical to that generated by Π_1 in the first system (see Fig. 7.2) and, hence, the two systems generate identical scan fields and scan patterns.

The abovementioned modifications bases on the following replacements:

- The refractive index n_1 of the first prism Π_1 is replaced by $n_1' = n_2$,
- The vertex angle α_1 of the first prism Π_1 is replaced by α_1' so that $\tan \alpha_1' = n_2 \sin \Theta_3 / (n_2 \cos \Theta_3 - 1)$, and
- The thickness d_1 of the first prism Π_1 is replaced by $d_1' = \Delta z_3 + d_1 + d_{\text{air}}$.

Here, the parameters Θ_3 and Δz_3 are given by Eqs. (7.19c) and (7.19d), respectively, which describe the half-vertex angle of the cone 3 and the location of the vertex of the cone on the z axis. As a consequence of the selection, the point of incidence on the front surface of the first prism Π_1' in Fig. 7.3 is now located at $z = \Delta z_3$.

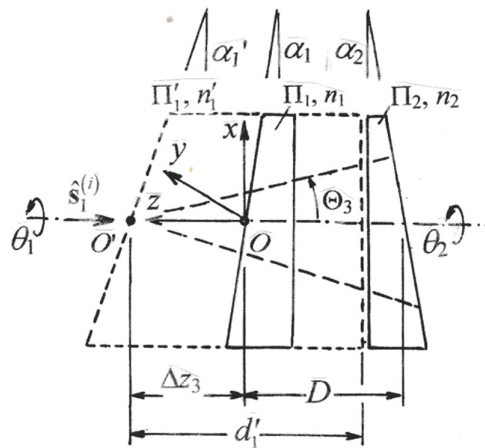


Figure 7.3 Two prism scanning systems: prisms Π_1 and Π_2 (both in solid line) and prisms Π_1' (in dashed line) and Π_2 (in solid line) may produce identical scan fields and patterns under the same control law.

Since the increase of thickness of the first prism and no change in the location of the origin point O on the axis of prisms rotation, so the two prisms Π'_1 and Π_2 are now in sliding contact that still allows the rotations of the two prisms according to their respective driving functions.

In reference to the formation of the conic-sections scan patterns [see the Section 2.2], we may express the position vector \mathbf{r}_{22} for the intersection of cone 3 and the surface 22 of the second prism Π_2 in the form

$$\mathbf{r}_{22} = (0, 0, \Delta z_2) - \frac{d_{12}}{B} (\tan \Theta_3 \cos \theta_1, \tan \Theta_3 \sin \theta_1, 1) \quad (7.20)$$

where $d_{12} = (d_1 \tan \Theta_1 + d_{\text{air}} \tan \Theta_2 + d_2 \tan \Theta_3) / \tan \Theta_3$ and $B = \tan \Theta_3 \tan \alpha_2 \cos(\theta_2 - \theta_1) - 1$.

The next step is a generalization of the above results from a single ray incidence to a bundle of rays, i.e., to the case of a light beam incidence.

If the ray passing through the prism scanner is considered as the axis of the beam of incidence, then the parameter \mathbf{r}_{22} in Eq. (7.20) represents the locus of the central points of the scanning spot. To evaluate the influence of the beam profile on \mathbf{r}_{22} , our attention returns to the scanning arrangement in Fig. 7.3 for a few adjustments in a way that the specification parameters of the first prism Π'_1 remain the same as the first prism Π_1 in the normal model, except

- The thickness of the first prism Π'_1 is $d'_1 \rightarrow d_1$, which implies that we are dealing with the limiting case of the air gap $d_{\text{air}} \rightarrow 0$;
- The incidence to the first prism Π'_1 is a beam described by Eq. (7.8).

After a long algebraic manipulations, the generalized express for the position vector \mathbf{r}_{22} takes the form

$$\mathbf{r}_{22} = (\xi - z_{11}, \eta - z_{11}, \Delta z_2) - \frac{d_{12} + f(\xi, \eta)}{B} (\tan \Theta_3 \cos \theta_1, \tan \Theta_3 \sin \theta_1, 1), \quad (7.21)$$

where $z_{11} = (\xi \cos \theta_1 + \eta \sin \theta_1) \tan \alpha_1 \tan \Theta_1$, and $f(\xi, \eta) = [(\xi \cos \theta_1 + \eta \sin \theta_1) \tan \Theta_1 \cos(\theta_2 - \theta_1) - (\xi \cos \theta_2 + \eta \sin \theta_2)] \sin \alpha_2$.

On substituting from Eq. (7.21) into Eq. (7.16), the scan pattern can be expressed parametrically as

$$\begin{pmatrix} X \\ Y \end{pmatrix} = - \begin{pmatrix} \xi - z_{11} \\ \eta - z_{11} \end{pmatrix} + \frac{\Delta z_3 + f(\xi, \eta)}{B} \begin{pmatrix} \tan \Theta_3 \cos \theta_1 \\ \tan \Theta_3 \sin \theta_1 \end{pmatrix} + \left[P + \Delta z_2 - \frac{d_{12} + f(\xi, \eta)}{B} \right] \begin{pmatrix} F_X(\theta_1, \theta_2) \\ F_Y(\theta_1, \theta_2) \end{pmatrix}, \quad (7.22)$$

or, more concisely as

$$\mathbf{R} = X + iY = -\rho_{10} + z_{11}(1+i) + \frac{\Delta z_3 + f(\xi, \eta)}{B} \tan \Theta_3 \exp(i\theta_1) \\ + \left[P + \Delta z_2 - \frac{d_{12} + f(\xi, \eta)}{B} \right] \frac{\sin \alpha_1 (\cos \alpha_1 - \sqrt{n_1^2 - \sin^2 \alpha_1}) \exp(i\theta_1) + A \sin \alpha_2 \exp(i\theta_2)}{\sqrt{n_2^2 - n_1^2 + [\sin^2 \alpha_1 + \cos \alpha_1 \sqrt{n_1^2 - \sin^2 \alpha_1}]^2} + A \cos \alpha_2},$$

where $\rho_{10} = \xi + i\eta$. (7.23)

7.2.4 Approximate expressions of scan patterns

To expand a tedious expression into a power series and then examine the predictions of its first several terms is a generally accepted technique in geometrical optics, from which we may gain some insight into the predictions of the exact formulation and also some explicit formulas for approximate computations.

This subsection examines the different order expansions for the exact ray-tracing solution to Risley prism pairs shown in Eq. (7.23).

A. Third-order approximation

After replacing all the sines and cosine of angles in the exact solution Eq. (7.23) with the first two terms of their power expansion, the resultant equations, in whatever form they are given, represent the results of *third-order theory*. Thus, after ignoring the terms of an order higher than α^3 in the power expansion of Eq. (7.23), we find the following expression containing the first- and third-order terms of the power expansion:

$$\mathbf{R}_3 = \mathbf{R}_{1F} + P \left\{ \begin{aligned} & \left[\frac{3n_1^3 - 6n_1^2 + 2n_1 + 3}{6n_1(n_1 - 1)^2} \delta_1^3 + \frac{2n_2 - 1 + n_2 \exp[2i(\theta_2 - \theta_1)]}{2(n_2 - 1)} \delta_1 \delta_2^2 \right] \exp(i\theta_1) \\ & + \left[\frac{2n_2 + 1 + n_2 \exp[2i(\theta_2 - \theta_1)]}{2n_2} \delta_1^2 \delta_2 + \frac{3n_2^2 - 3n_2 + 2}{6n_1(n_1 - 1)^2} \delta_2^3 \right] \exp(i\theta_2) \end{aligned} \right\} + \mathbf{R}_{3N},$$

(7.24)

where \mathbf{R}_{1F} represents the so-called J&W formula as shown in Eq. (7.6), and \mathbf{R}_{3N} represents the contributions of the scanning geometry parameters (D , D_n) and the incident beam parameters (ξ , η) to the field structure. We may express \mathbf{R}_{3N} as

$$\mathbf{R}_{3N} = -\rho_{10} - \left\{ -g(\theta_1) \frac{\exp(i\theta_1)}{n_1(n_1 - 1)} \delta_1^2 + g(\theta_2) \left[\frac{\exp(i\theta_1)}{n_2} \delta_1 + \frac{\exp(i\theta_2)}{n_2 - 1} \delta_2 \right] \delta_2 \right\} \\ + D_n \left\{ \begin{aligned} & \left[1 + \frac{2n_1^2 - 3n_1 + 3}{6n_1^2(n_1 - 1)^2} \delta_1^2 + \frac{n_2 + 1}{n_2(n_2 - 1)} \delta_1 \delta_2 \cos(\theta_2 - \theta_1) \right] \exp(i\theta_1) \\ & + \frac{\delta_2^2 \cos(\theta_2 - \theta_1)}{n_2 - 1} \exp(i\theta_1) \end{aligned} \right\} \delta_1, \quad (7.25)$$

where $g(\theta) = x_0 \cos \theta + y_0 \sin \theta$.

The third-order approximation shown in Eq. (7.24) is valid in both the near- and far-field regions. Since the term \mathbf{R}_{3N} represents contributions to the scan pattern as observed in the near-field region and, therefore, remove the term \mathbf{R}_{3N} from Eq. (7.24) in the far-field region computations.

B. Second-order approximation

After all of the terms of an order higher than δ^2 in Eq. (7.25) are discarded, we obtain the second-order approximation to the exact solution that is valid in both the near- and far-field regions and can be expressed in the form

$$\mathbf{R}_2 = \mathbf{R}_{1F} - \rho_{10} + \left\{ \begin{aligned} &\delta_1 \left[D_n - \frac{\delta_1}{n_1(n_1-1)^2} g(\theta_1) \right] \exp(\mathbf{i}\theta_1) \\ &+ \delta_2 \left[\frac{\exp(\mathbf{i}\theta_1)}{n_2} \delta_1 + \frac{\exp(\mathbf{i}\theta_2)}{n_2-1} \delta_2 \right] g(\theta_2) \end{aligned} \right\}. \quad (7.26)$$

Remove the terms ρ_{10} and D_n from Eq. (7.26) in far-field region computations.

C. First-order approximation

After all the terms of an order higher than δ^1 in Eq. (7.26) are discarded, there remains the first-order approximation to the exact solution that is valid in both the near- and far-field regions and can be expressed in the form

$$\begin{aligned} \mathbf{R}_1 &= \mathbf{R}_{1F} - \rho_{10} + D_n \delta_1 \exp(\mathbf{i}\theta_1) \\ &= P[\delta_1 \exp(\mathbf{i}\theta_1) + \delta_2 \exp(\mathbf{i}\theta_2)] - \rho_{10} + D_n \delta_1 \exp(\mathbf{i}\theta_1). \end{aligned} \quad (7.27a)$$

In case the pattern is scanned out by a single ray collinear with the z axis, i.e. when $\rho_{10} = 0$, Eq. (7.27) reduces to the form

$$\mathbf{R}_1 = P \left[\delta_1 \left(1 + \frac{D_n}{P} \right) \exp(\mathbf{i}\theta_1) + \delta_2 \exp(\mathbf{i}\theta_2) \right]. \quad (7.27b)$$

In the far-field region, Eqs. (7.26) and (7.27) reduce to the J&W formula shown in Eq. (7.7). This outcome implies that the validity of the J&W formula is restricted by two conditions, i.e., the thin-prism condition and the far-field-region application condition.

Finally, remove the terms ρ_{10} and D_n from Eqs. (7.26) and (7.27) in far-field region computations.

D. Numerical comparison of the predictions of different solutions

The curves in Figs. 7.4(a)–4(d) are plotted from Eqs. (7.18), (7.24), (7.25), (7.26), and (7.27) for a comparison of the scan patterns predicted by the exact solution and by the approximate theories under the conditions of a single ray incidence to the Risley prism furnished by two identical prisms with the prism

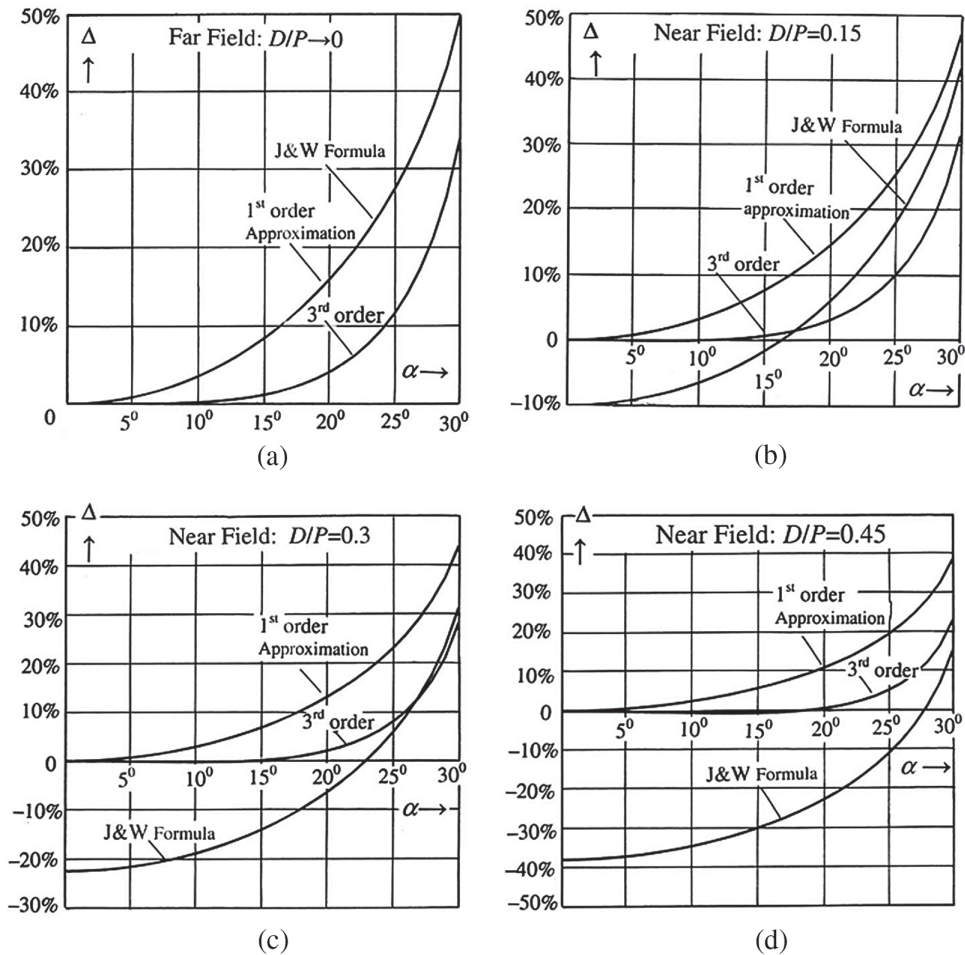


Figure 7.4 Curves plotted from Eqs. (7.18), (7.24), (7.25), (7.26), and (7.28), under the condition of $\theta_1 = \theta_2 = 0$, i.e., when Risley prism at rest, for a comparison of the percentage difference $\Delta(\%)$ in the calculations of the patterns scanned out by a single ray through Risley prism having two identical prisms of index $n_1 = n_2 = 1.5$ and the prism angle of $\alpha = 0^\circ \dots 30^\circ$ displayed on the plane in the far-field region ($D/P \rightarrow 0$) and planes at distances $D/P = 0.15, 0.3$, and 0.45 in the near-field region.

angle $\alpha = 0^\circ \dots 30^\circ$ and refraction index $n_1 = n_2 = 1.5$. Scan patterns are displayed either on the plane in the far-field region ($D/P \rightarrow 0$) or on planes in the near-field region at different distances $D/P = 0.15, 0.3$, and 0.45 .

Figures 7.4(a)–4(d) show a comparison under the condition of $\theta_1 = \theta_2 = 0$, i.e., when the two prisms at their rest positions. The two curves in 7.4(a) show the percentage difference $\Delta(\%)$ between the predictions of approximate theories of different order compared with the predictions of the exact solution. In the far-field region, the J&W formula, the first- and

second-order approximations give the same numerical results and can therefore be shown by one curve to compare with the curve plotted from Eq. (7.24) for the third-order theory.

Numerical results are also listed in Table 7.2, and we see that the scan pattern predicted by the first- and second-order theories may have $\sim 1\%$ maximum error when the prism angle $\alpha = 5^\circ$ as compared with the prediction of the exact solution, whereas under the same condition, the error reduces drastically to $\sim 0.01\%$ for the prediction by the third-order theory. The curves in Figs. 7.4(b)–4(d) show a comparison of scan patterns displayed on the planes located in the near-field range. Similar conclusions can be drawn that the third-order approximation has a much higher accuracy than predictions by the first-order theory.

A line scan can be produced by two identical and counter-rotated thin prisms at equal velocities, i.e., when the power of the prisms $\delta_1 = \delta_2 = \delta$ and the angular frequencies $\omega_1 = -\omega_2$. [7.18,7.25] In this case, Eqs. (7.6) and (7.27b) reduce, respectively, to the forms

$$X = 2P\delta \cos \theta_1, \quad Y = 0 \quad (7.28a)$$

and

$$X = P\delta \left(2 + \frac{D_n}{P} \right) \cos \theta, \quad X = D_n \delta \sin \theta. \quad (7.28b)$$

Figures 7.5(a) and 7.5(b) show that an exactly straight line segment scanned out is merely the prediction of the J&W formula and the linearity of the scanning spot motion [i.e., the LIN parameter, see Eq. (1.25)] is zero because of the minimum velocities of the scanning spot $V_{\min} = 0$ at the center of the line scan. Besides, all the theories predict a long elliptical pattern in the near-field region, and in the far-field region, the exact solution and the third-order theory predict a decorative scan curve in the shape of a bow-tie, as shown in Fig. 7.5(a) and 7.5(b), respectively.

The distortions of the scanning spot on the observation plane in the position normal to the z axis [see Fig. 7.1] are plotted from the third-order approximation in Eqs. (7.24) and (7.25). Computed results are shown in

Table 7.2 Percentage error of the approximate formulas Eqs. (7.24), (7.26), and (7.28) of different orders as compared with the predictions of the exact solution in Eq. (7.18) under the conditions of the prism angle $\alpha_1 = \alpha_2 = \alpha$, indices $n_1 = n_2 = n = 1.5$ and angular positions of the two prisms $\theta_1 = \theta_2 = 0$.

$\alpha =$	0°	5°	10°	15°	20°	25°	30°
First- and second-order approximations	0	0.9(%)	3.7(%)	8.5(%)	16.1(%)	27.9(%)	51.3(%)
Third-order approximation	0	0.01(%)	0.23(%)	1.2(%)	4.2(%)	11.9(%)	35.8(%)

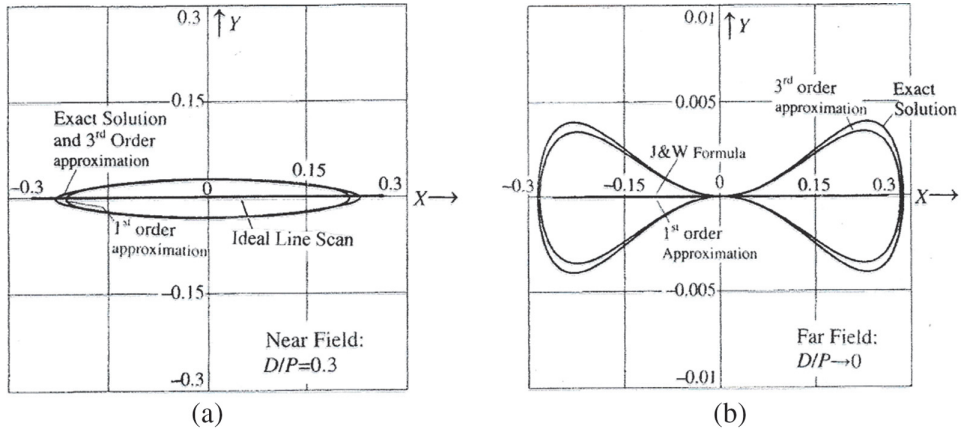


Figure 7.5 Comparison of the distortions in the line scan patterns produced by two counter-rotated thin prisms at equal angular velocities, i.e., $m = \omega_2 / \omega_1 = -1$. The prisms are identical with index $n = n_1 = n_2 = 1.5$ and the prism angle $\alpha = \alpha_1 = \alpha_2 = 15^\circ$: (a) Distortions in the line scan patterns displayed on planes located in the near-field region and (b) Distortions in the far-field region.

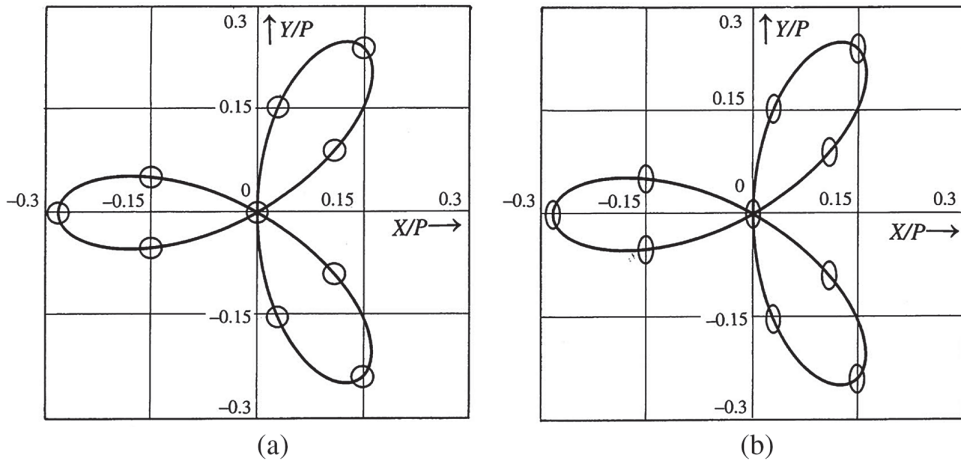


Figure 7.6 Far-field region scan patterns predicted by the third-order theory showing the scanning spot along the three-petal-rose curve produced by a pair of counter-rotated prisms of the same parameters: $n_1 = n_2 = n = 1.5$, the prism angle $\alpha_1 = \alpha_2 = \alpha = 15^\circ$, the angular frequency ratio $m = \omega_2 / \omega_1 = -2$ and the beam of incidence to this prism scanner with (a) a circular profile of radius $0.015P$ and with (b) an elliptical profile with the major and minor axes ($0.02P$, $0.01P$).

Figs 7.6(a) and 7.6(b) for beams with the circular and the elliptical profiles, respectively. A close view of the scanning spot profiles in different locations along the scan path reveals that no distinct scanning spot rotation and deformation can be observed when the spot is tracing along the

three-petal-rose curve produced by a pair of prisms with the same parameters: $n_1 = n_2 = n = 1.5$ and the prism angle $\alpha_1 = \alpha_2 = \alpha = 15^\circ$, but they are counter-rotated at an angular frequency ratio $m = \omega_2/\omega_1 = -2$. In general, scanning spot deformations are unavoidable when the scanning beam lands on the observation plane in a sloping position or, more specifically, hitting the observation plane with large angle of incidence.

Finally, comparison of accuracy between the predictions of first, third-order approximations and non-paraxial raytracing results has been studied experimentally by Y. Lu and Y. Zhou in [7.26].

7.3 Ray Deviation Power of Risley Prisms

This section considers the power of ray refraction by the Risley prism pairs in different configurations, including the following topics:

- Definition of the four types of Risley prism arrangement,
- The maximum and minimum angles of ray deviation, and
- The total internal refraction in Risley prism pairs and failure (i.e., the blind zone) analysis.

7.3.1 Standard analytic expressions of ray-tracing results for Risley prism pairs in different configurations

Figure 7.7 is a schematic diagram illustrating the four different configurations of Risley prisms, in which prisms Π_1 and Π_2 may have different indexes n_1 and n_2 and different apex angles α_1 and α_2 , but their principal sections are right angled triangles, for which the three sides can be defined in reference to their opening angles. For example, the symbol V is used to represent the side adjacent to the apex angle that is vertical to the z -axis, and the symbol T is used for the hypotenuse that is sloped to the z -axis. This nomenclature is illustrated on the left of Fig. 7.7 that allows us to describe the four configurations shown in Fig. 7.7(a) by the combination of the five symbols T, V, -, V and T, where the symbol “-” represents the air gap between the two prisms, and TV-VT implies a Risley prism pair in which the input surface of the first prism is sloped, the output surface is vertical followed by an air gap to the second prism with a vertical input surface and a sloped output surface. Making use of these symbols, we have a system in the VT-VT configuration [see, Fig. 7.7(b)] if the first prism Π_1 in Fig. 7.7(a) is turned 180° around the y axis. The four different configurations of the two wedge-prism systems are shown in Figs. 7.7(a)–7(d), i.e.,

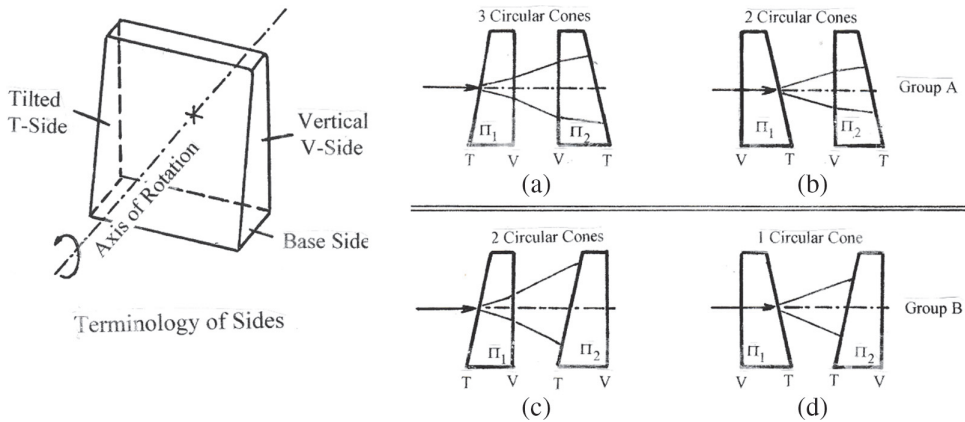


Figure 7.7 Risley prisms in four different configurations, in which symbol V means the prism surface vertical to the axis of rotation, and symbol T for the surface inclined at an angle to the axis. The (a) and (b) configurations can be classified in the group A, (c) and (d) in the group B according to the structural analysis of the scan fields they may produce inside the device.

TV - VT, VT - VT, TV - TV, and VT - TV.
 Model A-1 Model A-2 Model B-1 Model B-2

Further, we may group these four configurations into two groups according to the field distributions inside the prism pairs. In the group A, there are the TV-VT and VT-VT configurations, as shown in Figs. 7.7(a) and 7.7(b), and the configurations TV-TV and VT-TV in the Figs. 7.7(c)–7(d) are the in the group B, for which two groups of expressions are found for an explicit description of the scan fields produced by the four different configurations. This is possible due mainly to the fact that the main function of the first prism Π_1 in the four configurations is generalization of a circular cone, regardless to whether the first surface of Π_1 is vertical or inclined at an angle to the axis of rotation. Generalization of desirable scan patterns, other than a circular cone, mainly relies on the control law of the second prism Π_2 or, more specifically, on the direction and speed of the rotation of the second prism Π_2 , i.e., the TV and VT arrangements, as illustrated in Figs. 7.7(a)–7(b) and Figs. 7.7(a)–7(b) for the Groups A and B, respectively, so we may call the four configurations listed above as Model A-1, A-2, B-1, and B-2, respectively.

To this point, conclusion can be drawn with confidence that two groups of expressions are sufficient to describe the scan fields produced in front of the Risley prism pairs of different configurations, in which the A-1 configuration has been considered in Section 7.2, and we are now in the position to consider A-2 configuration, as shown in Fig. 7.7(b).

Assume the first prism Π_1 in A-2 is now in the position of θ_1 , the first surface of Π_1 is always vertical to z -axis as shown by its normal vector

$\hat{\mathbf{n}}_{11} = (0, 0, 1)$, and the second surface of Π_1 is inclined at an angle α_1 to z -axis as shown by its normal vector

$$\hat{\mathbf{n}}_{12} = (-\sin \alpha_1 \cos \theta_1, -\sin \alpha_1 \sin \theta_1, \cos \alpha_1).$$

The next step is an application of vector-based Snell's law [see Eq. (7.12)] to specify the ray refraction at the second surface of Π_1 , which is now rotating and scanning out a circular cone around the z -axis with the half-vertex angle, given by

$$\Theta_{1(A2)} = \arctan \frac{(-n_1 \cos \alpha_1 + \sqrt{1 - n_1^2 \sin^2 \alpha_1}) \sin \alpha_1}{-n_1 \sin^2 \alpha_1 - \cos \alpha_1 \sqrt{1 - n_1^2 \sin^2 \alpha_1}}, \quad (7.29)$$

where we attached the subscript 1(A2) to the symbol Θ for the half-vertex angle of the circular cone to stress its dependence on prism Π_1 in system of A-2 configuration.

It is interesting to compare the computed results of $\Theta_{1(A2)}$ from Eq. (7.29) with Θ_2 from Eq. (7.19c), where Θ_2 is the half-vertex angle Θ_2 of the second circular cone produced by the first prism Π_1 in the A-1 configuration. Assume the first prism in the A-1 and A-2 configurations is identical, i.e., $n_{1(A1)} = n_{1(A2)} = n_1$ and $\alpha_{1(A1)} = \alpha_{1(A2)} = \alpha_1$, computed results for this comparison show that under the conditions of $n_1 = 1.5$ and $\alpha_1 = 15^\circ$, we obtained $\Theta_2 = 7.61^\circ$ and $\Theta_{1(A2)} = 7.84^\circ$ and their percentage difference is 3.0%. For infrared systems using silicon prisms, [7.27] we may consider a system of $n_1 = 4.0$ and $\alpha_1 = 3.0^\circ$ and obtain $\Theta_2 = 9.04^\circ$ and $\Theta_{1(A2)} = 9.08^\circ$ and their percentage difference is 0.5%, from which we see the effect of turning the first prism 180° around the vertical axis in a system may not exert a significant influence to the scan field. Significant influence may be seen when prism opening angle $\alpha_1 > 30^\circ$. We obtained the same numerical results in the comparison between B-1 and B-2.

However, in the meantime, we see the possibility of that the A-1 and A-2 configurations may produce the same scan field if the first prisms in the A-1 and A-2 configurations scan out circular cones that have the same vertex angle. This requirement can be met by a modification of the refractive index n_1 of the first prism in the A-2 model based on the solution of the equation of compatibility $\Theta_{1(A2)} = \Theta_{2(A1)}$, to express which more explicitly, we may consider that all of the expressions to be developed for the A-2 model can be obtained from the formulations for the A-1 model as shown in the Table 7.1 and in Eq. (7.14)–(7.23) if the refractive index n_1 in all of the expressions for the A-1 model is replaced by

$$\sqrt{\sin^2 \alpha_1 + [(1 - n_1) \cos \alpha_1 - \sqrt{1 - n_1^2 \sin^2 \alpha_1}]^2}. \quad (7.30)$$

Table 7.3 The coefficients (a_1 , a_2 , a_3) in Eq. (7.31) for the direction cosines of the ray emergent from the Risley prism in the group A configurations.

A-1 or the TV-VT Configuration [Fig. 7.7(a)]	A-2 or the VT-VT Configuration [Fig. 7.7(b)]
$a_1 = \sin \alpha_1 (\cos \alpha_1 - \sqrt{n_1^2 - \sin^2 \alpha_1})$ (T7.3.1)	$-\sin \alpha_1 (n_1 \cos \alpha_1 - \sqrt{1 - n_1^2 \sin^2 \alpha_1})$ (T7.3.3)
$a_2 = -\sqrt{n_2^2 - n_1^2 + [\sin^2 \alpha_1 + \cos \alpha_1 \sqrt{n_1^2 - \sin^2 \alpha_1}]^2}$ (T7.3.2)	$-\sqrt{n_2^2 - 1 + [n_1 \sin^2 \alpha_1 + \cos \alpha_1 \sqrt{1 - n_1^2 \sin^2 \alpha_1}]^2}$ (T7.3.4)
$a_3 = F_A(\theta_1, \theta_2) + \sqrt{1 - n_2^2 + F_A^2(\theta_1, \theta_2)}$ where $F_A(\theta_1, \theta_2) = -a_1 \sin \alpha_2 \cos(\theta_2 - \theta_1) + a_2 \cos \alpha_2$ (T7.3.5)	
Useful identities $k_{2A}^2 + l_{2A}^2 + m_{2A}^2 = 1$ and $a_1^2 + a_2^2 = n_2^2$ (T7.3.6)	

On substituting from Eq. (7.30) into Eq. (7.14), the direction cosines of the field produced by Risley prism of the A-2 configuration are expressible in a form similar to those shown in Eq. (7.14) for the Risley prism of the TV-VT (i.e., the A-1) configuration. Therefore, the expressions for the two scanners in Group A may be expressed more explicitly in one form as

$$\left. \begin{aligned} k_{2A} &= a_1 \cos \theta_1 + a_3 \sin \alpha_2 \cos \theta_2, \\ l_{2A} &= a_1 \sin \theta_1 + a_3 \sin \alpha_2 \sin \theta_2, \\ m_{2A} &= -\sqrt{1 - k_{2A}^2 - l_{2A}^2} \end{aligned} \right\} \quad (7.31)$$

and, furthermore, we have $m_{2A} = a_2 - a_3 \cos \alpha_2$, where the coefficients (a_1 , a_2 , a_3) are shown by Eqs. (T7.3.1) to (T7.3.5) in Table 7.3.

Similarly, the prism systems in the TV-TV and VT-TV (i.e., B-1 and B-2) configurations as shown in Figs. 7.7(c) and 7.7(d) can be considered as the two members in the Group B, because the direction cosines (k_{2B} , l_{2B} , m_{2B}) of the rays emerging from these two systems can be expressed in the same forms as

$$\left. \begin{aligned} k_{2B} &= b_1 \cos \theta_1 - b_3 \sin \alpha_2 \cos \theta_2, \\ l_{2B} &= b_1 \sin \theta_1 - b_3 \sin \alpha_2 \sin \theta_2, \\ m_{2B} &= -\sqrt{1 - k_{2B}^2 - l_{2B}^2} \end{aligned} \right\} \quad (7.32)$$

and, furthermore, we have $m_{2B} = -\sqrt{1 - n_2^2 + (b_2 + b_3 \cos \alpha_2)^2}$, where the coefficients (b_1 , b_2 , b_3) are shown by Eqs. (T7.4.1) to (T7.4.5) in the Table 7.4.

Finally, the subscript 2A and 2B attached to the direction cosines (k_{2A} , l_{2A} , m_{2A}) and (k_{2B} , l_{2B} , m_{2B}) to stress their relationship with two-element Risley prisms.

7.3.2 Ray deviation angle of Risley prism pair and total-internal-reflection-induced blind zone in the scan field

The Risley prisms are equivalent to a single prism of variable power, [7.18,7.19] and when the prisms are in parallel, the power is twice that of either

Table 7.4 The coefficients (b_1 , b_2 , b_3) in Eq. (7.32) for the direction cosines of the ray emergent from the Risley prism in the group B configurations.

B-1 or the TV-TV Configuration [Fig. 7.7(c)]	B-2 or the VT-TV Configuration [Fig. 7.7(d)]
$b_1 = \sin \alpha_1 (\cos \alpha_1 - \sqrt{n_1^2 - \sin^2 \alpha_1})$ (T7.4.1)	$-\sin \alpha_1 (n_1 \cos \alpha_1 - \sqrt{1 - n_1^2 \sin^2 \alpha_1})$ (T7.4.3)
$b_2 = \sqrt{1 - n_1^2 + [\sin^2 \alpha_1 + \cos \alpha_1 \sqrt{n_1^2 - \sin^2 \alpha_1}]^2}$ (T7.4.2)	$n_1 \sin^2 \alpha_1 + \cos \alpha_1 \sqrt{1 - n_1^2 \sin^2 \alpha_1}$ (T7.4.4)
$b_3 = F_B(\theta_1, \theta_2) + \sqrt{n_2^2 - 1 + F_B^2(\theta_1, \theta_2)}$ where $F_B(\theta_1, \theta_2) = b_1 \sin \alpha_2 \cos(\theta_2 - \theta_1) - b_2 \cos \alpha_2$ (T7.4.5)	
Useful identities $k_{2B}^2 + l_{2B}^2 + m_{2B}^2 = 1$ and $b_1^2 + b_2^2 = 1$. (T7.4.6)	

one, and the angle ϕ of deviation of the emerging ray from the incidence attains the maximum value ϕ_{\max} , and when the two components are opposed, the power reaches the lowest level, and then the angle of deviation attains the minimum value ϕ_{\min} . To show the dependence of power and direction of ray deviation on the angle between the components is the aim of this Subsection.

The next step is the use of the expressions listed in Tables 7.2 and 7.3 to calculate the total angle of deviation between the emergent and incident rays of the Risley prism, as illustrated in Fig. 7.8, in which the angle ϕ represents the angular difference between the emergent ray and the incident ray that is in the direction parallel and coincided with the z axis.

The total angle of deviation is the resultant deviation of ray trace of a ray through the combination of two prisms, we may therefore express the results derived from Eqs. (7.31) and (7.32) in the form

$$\phi = \arctan \frac{\sqrt{(k_q)^2 + (l_q)^2}}{m_q} (q = 2A, 2B), \quad (7.33)$$

which is plotted in Fig. 7.9(a)–7.9(c) to show the how the variable power of Risley prisms effects of the angle ϕ of the ray emerging from the systems of different configurations.

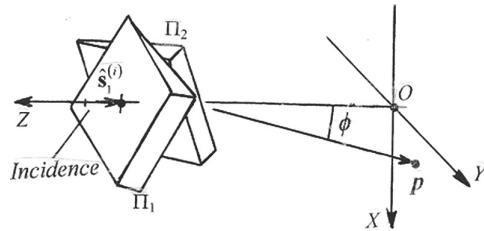


Figure 7.8 A pair of rotatable prisms is equivalent to a single prism of variable power as shown by the change the total angle ϕ of deviation between the emergent and incident rays when prisms rotated.

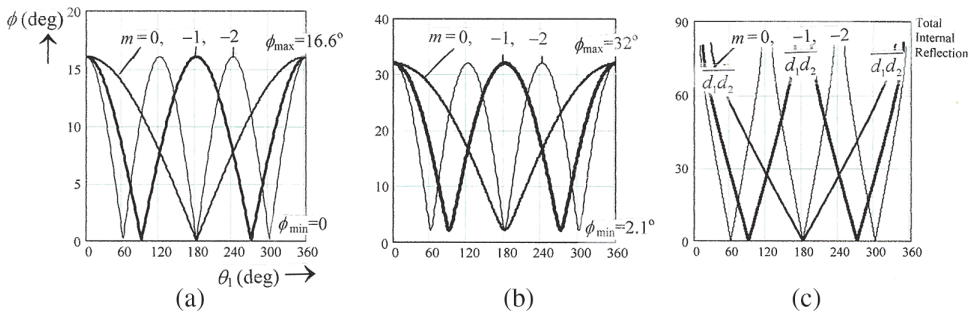


Figure 7.9 The variable ranges of the angle ϕ (i.e., the total angle of ray deviation) as a function of the rotation angle θ_1 of the first prism with the angular positions ratio $m = \theta_2/\theta_1 = 0, -1$ and -2 as a parameter, (a) The total angle of deviation for A-1 configuration with refractive indexes $n_1 = n_2 = n = 1.5$, $\alpha_1 = \alpha_2 = \alpha = 15^\circ$, (b) The total angle of deviation for B-1 configuration with the refractive indexes $n_1 = n_2 = n = 1.5$, $\alpha_1 = \alpha_2 = \alpha = 30^\circ$, (c) The total angle of deviation for A-1 configuration with refractive indexes $n_1 = n_2 = n = 4.0$ (silicon prisms for infrared applications), $\alpha_1 = \alpha_2 = \alpha = 9.5^\circ$.

A pair of rotatable prisms is equivalent to a single prism of variable power; if the two prisms rotate at constant speeds, then the power of the prism combination varies periodically, the parameter ϕ , i.e., the total angle of deviation of Risley prism, experiences periodical variation between the maximum and minimum angles, as shown by the symbols ϕ_{\max} and ϕ_{\min} in Fig. 7.9, in which the curve in Fig. 7.9(a) is plotted from Eq. (7.33) for the A-1 configuration [see. Fig. 7.7(a)], and $\phi_{\max} = 16.6^\circ$ and $\phi_{\min} = 0^\circ$ are found under the conditions of refractive indexes $n_1 = n_2 = n = 1.5$, and the prism angles $\alpha_1 = \alpha_2 = \alpha = 15^\circ$ and the angular positions ratio $m = \theta_2/\theta_1 = 0, -1$ and -2 . Similarly, Fig. 7.9(b) is plotted and shows that $\phi_{\max} = 32.0^\circ$ and $\phi_{\min} = 2.1^\circ$ for the B1 configuration [see. Fig. 7.7(c)], and it is seen that the value of ϕ_{\max} is greater than that shown in Fig. 7.9(a). This is because of the increase of the prism angle. Finally, we found that the maximum deviation angle ϕ_{\max} becoming unpredictable for the Risley prism in A-1 configuration when the refractive indexes of the prisms increase from 1.5 to 4.0, i.e., when the glass prisms are replaced by prisms using silicon material, which is typical in the applications of the Risley prism to the infrared region. In this application, the effect of total internal reflection may cut off the ray path to cease system operation as detailed in subsequent discussion.

A graphic analysis of the variation of the total deviation angle ϕ is shown in Fig. 7.10, which begins with the ray path diagram in Fig. 7.10(a) and it is seen that the angle ϕ attains the maximum or the minimum values when the two prism apexes are aligned or opposed, i.e., when the rotation angles of the two prisms $\theta_2 - \theta_1 = 0^\circ$ or $\theta_2 - \theta_1 = 180^\circ$, respectively. In the position of $\theta_2 - \theta_1 = 0^\circ$, the undesirable effect of the total internal reflection (TIR) [7.24] within one of the two prisms in the system may be developed and then cease the beam steering activity. This effect may considerably reduce the variation

of the total deviation angle ϕ and is considered as the major failure mode of the prism scanners.

The TIR occurs when the angle of incidence to a glass-to-air surface is greater than the critical angle ψ_c . For incident angles greater than ψ_c , the light is totally reflected back into the prism, no light is transmitted (see, e.g., p.9 of Ref. 7.7). In our case, the development of the TIR at the second surface 22, i.e., the glass-to-air surface of the second prism Π_2 in the V-T and T-V arrangements, is illustrated in Figs. 7.10(b) and 7.10(c), respectively. In general, prisms Π_1 and Π_2 may be different in material and we may use the symbols

$$\psi_{c1} = \arcsin(1/n_1) \text{ and } \psi_{c2} = \arcsin(1/n_2)$$

for the critical angle of the second surfaces of the prisms Π_1 and Π_2 , respectively,

Figure 7.10(a) shows the graphical analysis for system with the A-1 configuration [see Fig. 7.7(a)], in which the second surface 22 of the second prism Π_2 is tilted at an angle α_2 , and it is seen that when the incident angle reaches the critical angle, the transmitted light is traveling perpendicular to the normal \hat{n}_{22} (i.e., in parallel to the glass-to-air interface 22) and then the condition for TIR inside the second prism Π_2 , given by

$$\begin{aligned} \phi &= 90^\circ - \alpha_2 \text{ in general, and } \Theta_3 + \alpha_2 \geq \psi_{c2} \text{ for the spical case of} \\ \theta_1 = \theta_2 &= 0^\circ, \end{aligned} \quad (7.34a)$$

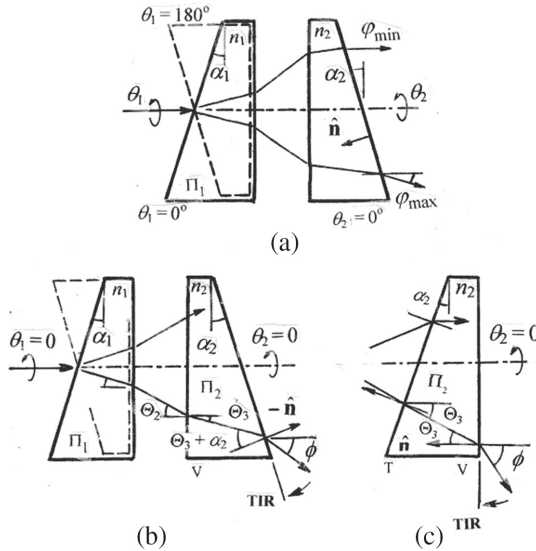


Figure 7.10 Illustrating the maximum and minimum angles ϕ_{\max} and ϕ_{\min} of the total angle of deviation between the ray of emergence and incidence. The first prism Π_1 has two positions at $\theta_1 = 0^\circ$ (solid line) and $\theta_1 = 180^\circ$ (dashed line). The second prism Π_2 has one position at $\theta_2 = 0^\circ$ (a) ϕ_{\max} when $\theta_1 = 0^\circ$, ϕ_{\min} when $\theta_1 = 180^\circ$ (b) Development of the total internal reflection (TIR) in the second prism in the A-1 configuration when $\theta_1 = \theta_2 = 0^\circ$ and $n_2 \gg 1$. (c) The total internal reflection (TIR) in the second prism in the B-1 configuration.

where Θ_3 can be found in Eq. (7.17c). Similarly, Fig. 7.10(c) is for system of the B-configurations [see Figs. 7.7(c) and 7.7(d)], in which the second surface 22 of the second prism Π_2 is perpendicular to axis of the second prism Π_2 , i.e., the tilted angle $\alpha_2 = 0$. After the deletion of α_2 in Eq. (7.34a), we obtain the condition for TIR inside the second prism Π_2 to occur expressible as

$$\phi = 90^\circ \text{ in general, and } \Theta_3 \geq \psi_{c2} \text{ for the spical case of } \theta_1 = \theta_2 = 0^\circ. \quad (7.34b)$$

After substituting from $\phi = 90^\circ - \alpha_2$ into Eq. (7.33), we obtain the following inequality for the A-1 configuration Risley prism [see Fig. 7.7(a)]

$$\sin \alpha_2 \sqrt{(k_{2A})^2 + (l_{2A})^2} \geq m_{2A} \cos \alpha_2, \quad (7.35a)$$

to determine the region of prism rotation, in which the TIR occurs and, hence, no light transmitted [i.e., the blind zone, see, e.g., $\overline{d_1 d_2}$ in Fig. 7.9(c)]. Similarly, for the B-configuration Risley prism [see Figs. 7.7(c) and 7.7(d)], from Eqs. (7.34b) and (7.33) we have the following inequality:

$$m_{2B} \leq 0. \quad (7.35b)$$

Expressions for direction cosines (k_{2A}, l_{2A}, m_{2A}) and (k_{2B}, l_{2B}, m_{2B}) for the Risley prism in the A- and B-configurations can be found from Eqs. (7.31)–(7.32) and their expressions are listed in Tables 7.3 and 7.4.

7.3.3 Influence of total internal reflection on the power of ray deviation by Risley prism

Figure 7.9(c) showed how the TIR in the second prism Π_2 affects the variation of total angle of deviation, and Figs. 7.10(b) and 7.10(c) illustrated the development of TIR in that prism Π_2 . However, Fig. 7.11 shows the TIR occurred inside the first prism Π_1 as well.

Figures 7.11(c) and 7.11(d) are supplementary to Figs. 7.10(b) and 7.10(c) for a schematic illustration of the TIR inside the second prism in the Risley prism.

The remaining part of this section considers TIR occurring at the glass-to-air interface of the first prism Π_1 with the prism angle α_1 and refractive index n_1 , as shown, respectively, in Figs. 7.11(a) and 7.11(b) for systems with the first prism Π_1 in the T-V and V-T configurations, for which a parameter α_c was introduced to express the TIR to occur inside the prism Π_1 when the power of Π_1 increases. For the T-V configuration in Fig. 7.11(a), the TIR inside Π_1 occurs when its prism angle

$$\alpha_1 \geq \alpha_c = \operatorname{arccot}(\sqrt{n_1^2 - 1} - 1), \quad (7.36a)$$

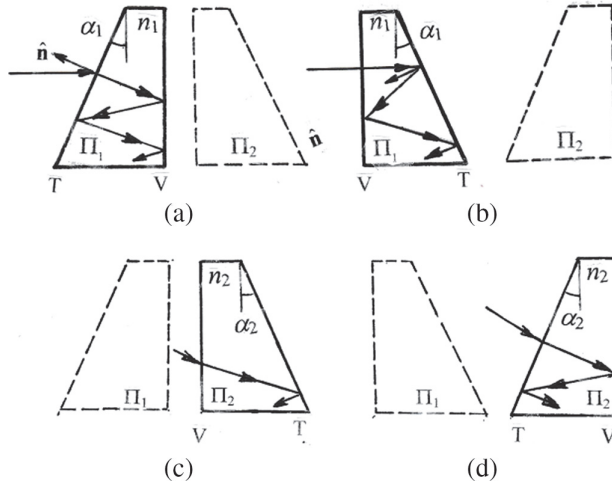


Figure 7.11 Geometry showing the ray traversing the Risley prism and the variation of the angle ϕ of the total angle of deviation of the rays emerging from this system. (a) TIR occurred inside the first prism Π_1 in A-1 configuration, (b) TIR occurred inside the first prism Π_1 in A-2 configuration, (c) TIR occurred inside the second prism Π_2 in A-1 configuration, (d) TIR occurred inside the second prism Π_2 in B-2 configuration,

which no limitation on the selection of α_1 if $n_1 \leq \sqrt{2}$. For the V-T configuration, we have

$$\alpha_1 \geq \alpha_c = \arcsin(1/n_1). \quad (7.36b)$$

Predictions of the above two expressions are shown by two curves in Fig. 7.12 with the numerical data of α_c marked on the curves for $n_1 = 1.5$ and 4.0. Comparison of the computed results reveals that the critical prism angle α_c of the Risley prism with the first component in the T-V configuration is much greater than that of the V-T configuration. This implies that the Risley prism shown in Figs. 7.7(a) and 7.7(c) are less sensitive to activate the TIR inside the first prism than the configurations shown in Figs. 7.7(b) and 7.7(d).

A comparison of the power of ray deviation for systems in different configurations is shown in Figs. 7.13(a) and 7.13(b) for systems having two identical prisms of prism angle $\alpha_1 = \alpha_2 = \alpha$ and indices $n_1 = n_2 = n = 1.5$ (glass prisms) and $n_1 = n_2 = n = 4.0$ (silicon prisms), respectively.

Computed results of Eqs. (7.31) and (7.32) for the difference $\Delta\phi_m = \phi_{\max} - \phi_{\min}$ are plotted in Figs. 7.13(a) and 7.13(b) as a function of the prism angle α , all the curves in which have a linear portion when the prism angle is small. In this portion the Risley prism of deferent configurations predict the same results expressible in the form shown in Eq. (7.6), which can be further expressed as

$$\Delta\theta_m = 2\alpha(n - 1). \quad (7.37)$$

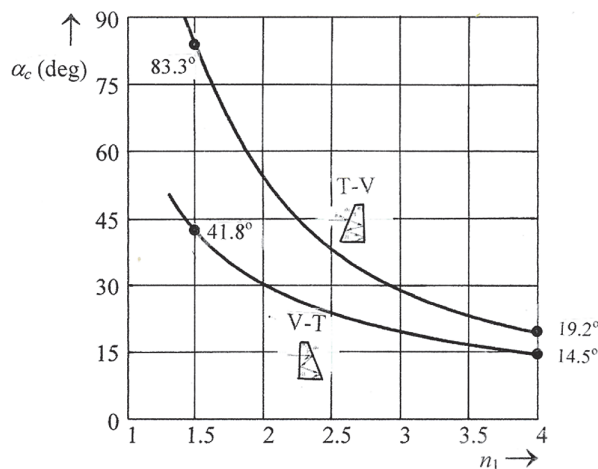
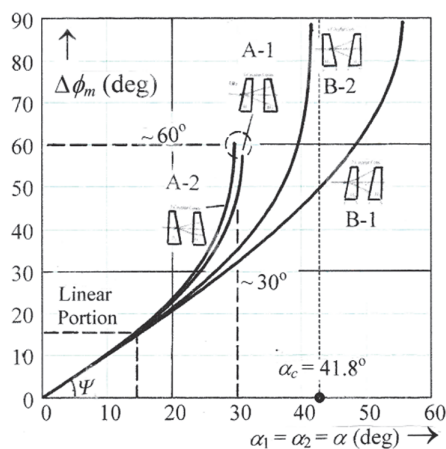
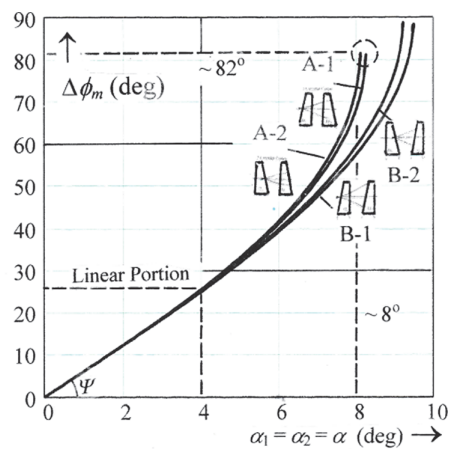


Figure 7.12 The critical prism angle α_c for the first component of the Risley prism as a function of the refractive index n_1 . For prism angle α_1 greater than α_c , no light transmitted, but reflected back totally into the prism.



(a) $n_1 = n_2 = n = 1.5$



(b) $n_1 = n_2 = n = 4.0$

Figure 7.13 Comparison of the maximum ray deviation angle $\Delta\phi_m = \phi_{\max} - \phi_{\min}$ for systems of different configuration under the conditions of two prisms with the same apex angle α and refractive index n . (a) $n = 1.5$ and (b) $n = 4.0$.

The difference of the maximum and minimum ray deviation angles $\Delta\phi_m = \phi_{\max} - \phi_{\min}$ predicted by the exact solution and the linear and third-order theories is summarized in Table 7.5. Comparing to the information presented in Table 7.2, the current table uses the average of the results obtained for the four configurations and has a larger region of the refractive index, whereas Table 7.2 was concentrated in a consideration of the A-1 configuration of the Risley prism.

Table 7.5 Comparison of the computed results of the maximum deviation angle $\Delta\phi_m$ predicted by different theories for the Risley prism under the conditions of the prism angle $\alpha_1 = \alpha_2 = \alpha$ and the refractive indices $n_1 = n_2 = n$.

n	α	First-Order Approximation vs. the Exact Solution ^(a)	Third-Order Approximation vs. the Exact Solution ^(b)
1.5	$\leq 15^\circ$ ^(c)	4.5 (%)	1.0 (%)
	$= 30^\circ$ ^(d)	24.3 (%)	6.4 (%)
4.0	$\leq 4.0^\circ$ ^(c)	4.2 (%)	0.03 (%)
	$= 8.0^\circ$ ^(d)	24.3 (%)	0.2 (%)

^(a) Average of the computed results of the exact solution of the four configurations A-1, A-2, B-1 and B-2.

^(b) Computed results of the configurations A-1.

^(c) In the linear portion.

^(d) Beyond the linear portion.

Finally, let us return to the curves plotted on Fig. 7.13 and find out the factor that restricts the amplitude of the total angle of deviation. The two curves labeled A-1 and A-2 in Fig. 7.13(a) are terminated at the point ($\alpha \sim 30^\circ$, $\Delta\phi_m \sim 60^\circ$), which indicates that at this point the tilted angle of the second surface of the second prism Π_2 is 30° and the light incident to this glass-to-air interface is at the critical angle ψ_{c2} because the ray refracted off this interface is in the direction of $\Delta\phi_m \sim 60^\circ$, that implies the transmitted ray is traveling in parallel to the interface or, more actually, the effect of total internal reflection terminates the possibility of further increasing of the ray deviation power of the Risley prism by increasing their prism angles. Similar conclusions can be drawn for the remaining curves in Figs. 7.13(a) and 7.13(b), in which the curves labeled B-2 in Fig. 7.13(a) is terminated when $\alpha \sim 41^\circ$, that is very close to the critical angle of $\alpha_c \sim 41.8^\circ$, as shown the curve label V-T in Fig. 7.12. In this case, the ray refracted off the first prism Π_1 may be able to hit the second prism Π_2 due to the large angle of ray deviation by Π_1 because its prism angle α near the critical value α_c as shown schematically in Fig. 7.14.

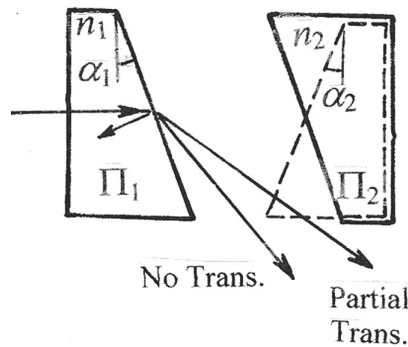


Figure 7.14 No or partial light transmitted. Failure of Risley prism due to the large angle of ray deviation by the first prism when its prism angle α near the critical value α_c .

Bibliography and Links

- [7.1] Prism definition. URL: <https://en.wikipedia.org/wiki/Prism>
- [7.2] Wedge prism definition. URL: https://en.wikipedia.org/wiki/Wedge_prism and https://spie.org/publications/tt48_525_wedge?SSO=1
- [7.3] Thin prism definition. URL: <https://in.answers.yahoo.com/question/index?qid=20130918035132AA42EqR>
- [7.4] M. Sanchez and D. Gutow, "Control laws for a three-element Risley prism optical beam pointer," *Proc. SPIE* **6304**, 630403 (2006).
- [7.5] M. Ostaszewski, S. Harford, N. Doughty, C. Hoffman, M. Sanchez, D. Gutow, and R. Pierce, "Risley prism beam pointer," *Proc. SPIE* **6304**, 630406 (2006).
- [7.6] P. J. Bos, H. Garcia, and V. Sergan, "Wide-angle achromatic prism beam steering for infrared countermeasures and imaging applications: solving the singularity problem in the two-prism design," *Opt. Eng.* **46**(11), 113001 (2007).
- [7.7] N. R. Smith, D. C. Abeysinghe, J. W. Haus, and J. Heikenfe, "Agile wide-angle beam steering with electrowetting micropisms," *Opt. Exp.*, **14**, 6557–6563 (2006).
- [7.8] B. D. Duncan, P. J. Bos, and V. Sergan, "Wide-angle achromatic prism beam steering for infrared countermeasure applications," *Opt. Eng.*, **42**, 1038–1047 (2003).
- [7.9] Y. Li, "Third-order theory of the Risley-prism-based beam steering system," *Appl. Opt.* **50**, 679–686 (2011).
- [7.10] G. F. Marshall, "Risley prism scan patterns," *Proc. SPIE* **3787**, 74–86 (1999).
- [7.11] C. Schwarze, "A new look at Risley prisms," *Photonics Spectral*, *Photonics Spectra*, Jun (2006). https://www.photonics.com/Articles/A_New_Look_at_Risley_Prisms/a25652
- [7.12] J. Kramer and D. Henderson, "Micro Beam Steering: Precision micro beam-steering systems simplify move to handheld instruments," *Laser Focus World*, Jun (2015). URL: <https://www.laserfocusworld.com/software-accessories/positioning-support-accessories/article/16551608/micro-beam-steering-precision-micro-beamsteering-systems-simplify-move-to-handheld-instruments>
- [7.13] E. Kiesler, "Out of the lab and into the world: the endoscopic laser scalpel," *Memorial Sloan Kettering Cancer Center blog* (Dec. 1, 2011); see <http://bit.ly/1AAFI5y>.
- [7.14] D. Henderson, "Bringing image-guided laser surgery to endoscopy," *Medical Design Technology* (Oct. 2013); see <http://bit.ly/1dAjnLE>.
- [7.15] G. Garcia-Torales, M. Strojnik, and G. Paez, "Risley prisms to control wave-front tilt and displacement in a vectorial shearing interferometer," *Appl. Opt.*, **41**, 1380–1384 (2002).

- [7.16] W.C. WargerII, S.A. Guerrera, and C.A. DiMarzio, "Toward a compact dual-wedge point-scanning confocal reflectance microscope," *Proceedings Volume 6443, Three-Dimensional and Multidimensional Microscopy: Image Acquisition and Processing XIV*; **644311** (2007)
- [7.17] H. Erfle, "Über die durch ein Drehkeilpaar erzeugte Ablenkung und über eine als Kennzeichen für die Beibehaltung des 'Hauptschnittes' dienende Sinusbedingung," *Zeitschrift für Physik* **1**, 57–81 (1920).
- [7.18] F. A. Rosell, "Prism scanners," *J. Opt. Soc. Am.* **50**, 521–526 (1960).
- [7.19] F. R. Jenkins and H. E. White, *Fundamentals of Optics*, 4th ed. (McGraw-Hill, 2001), Sec. 2.7.
- [7.20] A. Li, W. Yi, Q. Zuo, and W. Sun, "Performance characterization of scanning beam steered by tilting double prisms," *Opt. Express*, **24**, pp. 23543–23556, 2016.
- [7.21] A. Li, Y. Ding, Y. Bian, and L. Liu, "Inverse solutions for tilting orthogonal double prisms," *Appl. Opt.* **53**(17), 3712–3722 (2014).
- [7.22] V.-F. Duma, A. Vlaicu, and J.P.Rolland, "Advancements on galvanometer scanners for high-end applications," in *Design and Quality for Biomedical Technologies VII*, R. Raghavachai and R. Liangeeds., Proc. SPIE **8936**, doi: 10.1117/12.2038357, (2014)
- [7.23] M. Zohrabi, R. H. Cornak, and Juliet T. Gopinath, "Wide-angle non-mechanical beam steering using liquid lenses," **24**(21), *Opt. Exp.* 23798–23809 (2016).
- [7.24] Y. Zhou, S. Fan, Y. Chen, X. Zhou, and G. Liu, "Beam steering limitation of a Risley prism system due to total internal reflection," *Appl. Opt.* **56**, 6079–6086 (2017).
- [7.25] W. L. Wolfe, "Optical-mechanical scanning techniques and devices," in *The Infrared Handbook*, W. L. Wolfe and G. J. Zissis, eds. (Environmental Research Institute of Michigan, 1989), Chap. 10.
- [7.26] Y. Lu, Y. Zhou, M. Hei, and D. Fan, "Theoretical and experimental determination of steering mechanism for Risley prism systems," *App. Opt.*, **52**, 1389–1398 (2013).
- [7.27] URL: <https://refractiveindex.info/?shelf=main&book=Si&page=Aspn>